Identifying Majorana zero modes in vortex lattices using Fano factor tomography

Jiong Mei [●],[1,2] Kun Jiang [●],[1,2,*] and Jiangping Hu[1,3,4,†]

[1]*Beijing National Laboratory for Condensed Matter Physics and Institute of Physics, Chinese Academy of Sciences, Beijing 100190, China*
[2]*School of Physical Sciences, University of Chinese Academy of Sciences, Beijing 100190, China*
[3]*Kavli Institute of Theoretical Sciences, University of Chinese Academy of Sciences, Beijing 100190, China*
[4]*New Cornerstone Science Laboratory, Beijing 100190, China*

In this work, we investigate the tunneling characteristics of Majorana zero modes (MZMs) in vortex lattices based on scanning tunneling microscopy measurement. We find that zero bias conductance does not reach the quantized value owing to the coupling between the MZMs. On the contrary, the Fano factor measured in the high voltage regime reflects the local particle-hole asymmetry of the bound states and is insensitive to the energy splitting between them. We propose using spatially resolved Fano factor tomography as a tool to identify the existence of MZMs. In both cases of isolated MZM or MZMs forming bands, there is a spatially resolved Fano factor plateau at one in the vicinity of a vortex core, regardless of the tunneling parameter details, which is in stark contrast to other trivial bound states. These results reveal new tunneling properties of MZMs in vortex lattices and provide measurement tools for topological quantum devices.

I. INTRODUCTION

As building blocks for topological quantum computation [1], Majorana zero modes (MZMs) have received substantial attention in the past few decades, owing to their predicted non-Abelian statistics, topological protection, and robustness against environmental noise [2–4]. Owing to previous tremendous efforts, realizing MZMs in materials systems has gained great success, including superconducting proximitized topological insulators [5], 1D spin-orbit coupled superconducting nanowires [6–8], ferromagnetic Yu-Shiba-Rusinov chains [9,10], topological planar Josephson junctions [11–16], especially the connate topological superconductor in iron-based superconductors [17–21]. Among these platforms, vortex-bound states in iron-based superconductors [18–21] have shown to be a particularly promising pathway for implementing and studying MZMs. Recently, a large-scale, ordered MZM lattice has also been achieved in naturally strained LiFeAs, leading a pathway towards tunable and ordered MZM lattices [22]. In this work, we apply the current noise Fano factor method to the vortex lattices based on scanning tunneling microscopy (STM), which can be realized with the current state-of-the-art STM experiments [23–25] and find the Fano factor tomography providing an efficient way of identifying MZMs.

We begin by studying single vortices with different bound states using STM measurements. Our study shows that, despite the widely used differential conductance measurement, spatially resolved Fano factor tomography is an effective tool for distinguishing MZMs from other trivial bound states.

Previous literature [26] has noted that the Fano factor measured in the high voltage regime reflects the local particle-hole asymmetry of the bound state wave function. Consequently, the spatially resolved Fano factors near an MZM remain at a value of one due to the local particle-hole symmetry of its wave function. On the contrary, the breaking of this symmetry for other trivial zero-energy bound states results in a strong spatially oscillated Fano factor. We conducted an in-depth study on this phenomenon, and while providing the physical picture behind it, we point out that it is robust to the energy splitting between the bound states.

Theoretically, in the case of an isolated MZM, the tunneling conductance is expected to be quantized at zero energy [27,28], providing a hallmark for their identification. However, the anticipated quantization at zero energy is often deviated in experimental setups due to finite temperature and the presence of couplings between MZMs [29]. We proceed with studying MZM lattices and focus on the effects of MZM couplings in vortex lattices at zero temperature to comprehend their tunneling characteristics. Particularly, we investigate how MZM couplings suppress the differential conductance. Contrary to the differential conductance, the spatially resolved Fano factors exhibit lower sensitivity to the energy splittings among the MZMs. Hence, Fano factor tomography can reveal the presence of well-separated MBS in the vortex core region, even in the presence of coupling. Furthermore, we investigate the behavior of Fano factors measured in the high voltage regime when both single-electron tunneling and Andreev reflection processes coexist. Our findings reveal that Fano factor tomography can be effective only when Andreev reflections dominate, which necessitates working within the strong tunneling regime.

This paper is organized as follows. In Sec. II, we first review the concept of Fano factor and apply
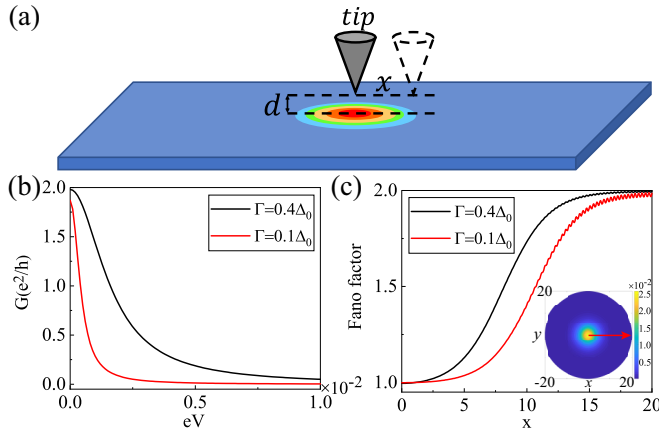
*jiangkun@iphy.ac.cn
†jphu@iphy.ac.cn

FIG. 1. (a) Scheme of a typical STM setup for measuring vortex bound states tunneling characteristics. The energy width Γ can be increased by decreasing the tip-sample distance (d), and the tip can be moved horizontally to obtain Fano factor tomography. (b) Differential conductance at the vortex core center of a Fu-Kane model. (c) Spatially resolved Fano factors measured in the high voltage regime (we set $eV_{\text{bias}} = 0.5\Delta_0$ in this case). The inset in (c) shows the MZM wave function, with arrows indicating the scanning directions. The slight oscillations of the Fano factor away from the vortex core are due to the finite bases cutoff in our numerical simulation.

this technique to single vortices in 2D superconductors. We then propose a simple Majorana toy model to understand the behavior of the Fano factor measured in different bound states and discuss the robustness of the Fano factor measured in the high voltage regime in Sec. III. In Sec. IV, we inevisigate the the tunneling characteristics of MZMs in vortex lattices. We examine the effect of the couplings between different MZMs to the tunneling conductance and show how Fano factor tomography can still serve as a valuable tool to identify the existence of a well-separated MZM in this case. We conclude with a discussion of the presented results in Sec. V. The paper is followed by six appendices that cover several technical details and supplementary information.

II. SINGLE VORTEX

To gain a complete understanding of the Fano factor tomography, we start with the tunneling characteristics of a single vortex in a 2D superconductor (SC) coupled with a metallic STM tip as depicted in Fig. 1(a). To model the STM experiment, we define the complete Hamiltonian $H_{\text{tot}} = H_T + H_S + H_{\text{tunnel}}$, which includes the coupling between the tip and the sample:

$$H_{\text{tunnel}} = \sum_{\sigma} t_{\text{tunnel}} \psi_{T,\sigma}^{\dagger} c_{j,\sigma} + \text{H.c.} \tag{1}$$

Here, the operator $\psi_{T,\sigma}$ annihilates an electron of spin σ at the apex of STM tip while $c_{j,\sigma}$ annihilates an electron of spin σ at site j of the 2D lattice. H_T is the Hamiltonian of the isolated metallic tip and H_S is the Hamiltonian of the grounded SC, which can be described by the following BdG Hamiltonian,

$$H_S = \begin{pmatrix} \hat{h} & \hat{\Delta} \\ \hat{\Delta}^* & -\sigma_y \hat{h}^* \sigma_y \end{pmatrix}, \tag{2}$$

where $\sigma_{x,y,z}$ are Pauli matrices acting in the physical spin space, and $\hat{\Delta}$ is the superconducting pair potential. We note that, for simplicity, the 2D superconductivity is used as a static input in all subsequent calculations. The Hamiltonian acts on a four-component Nambu spinor $\hat{\Psi}_j = (c_{j,\uparrow}, c_{j,\downarrow}, c_{j,\downarrow}^{\dagger}, -c_{j,\uparrow}^{\dagger})^T$. We assume a point contact of the sample-tip tunneling and use a wide-band approximation for the metallic tip. We fix $\hbar = 1$ and the unit length (lattice constant) $a = 1$ throughout. Tunneling events are thus characterized by the energy width $\Gamma = 2\pi \nu_T t_{\text{tunnel}}^2$, where ν_T is the density of states in the tip. The bias voltage V between the tip and the sample is taken into account in the chemical potential of the tip as $\mu_T = \mu + eV$.

The charge current flowing from the tip is $I(j, t_1) = -e\frac{d\hat{N}_T(t_1)}{dt_1}$, where $\hat{N}_T(t_1)$ is the number operator counting the electrons in the tip at time t_1 in the Heisenberg picture. In the DC regime, $I(j, t_1) = I(j)$ and the corresponding differential conductance is defined as $G = \frac{dI(j,eV)}{dV}$. Shot-noise is the zero-frequency limit of the time-symmetrized current-current correlator, $S = \int d(t_1 - t_2) S(t_1, t_2)$, given by $S(t_1, t_2) = \langle \delta I(t_1) \delta I(t_2) \rangle + \langle \delta I(t_2) \delta I(t_1) \rangle$ where $\delta I(t_1) = I(t_1) - \langle I(t_1) \rangle$. Hence, the spatially resolved Fano factor is defined as

$$F(j, eV) \equiv \frac{S(j, eV)}{2e|I(j, eV)|}. \tag{3}$$

These physical quantities can be calculated through the standard Keldysh formalism [26,30]. Specifically, when the STM tip tunnels into a pair of single orbital zero energy bound states $\phi_+ = [u_\uparrow(j), u_\downarrow(j), v_\downarrow(j), -v_\uparrow(j)]^T$ and its particle-hole partner, $\phi_- = \tau_y \sigma_y \mathcal{K} \phi_+(j)$, where $\tau_{x,y,z}$ are Pauli matrices acting in the particle-hole space and $\mathcal{K}$ denotes the complex conjugation, the Fano factor in the zero-temperature limit and high voltage regime, $eV \gg \Gamma_j$, with $\Gamma_j = \Gamma \sum_\sigma (|u_\sigma(j)|^2 + |v_\sigma(j)|^2)$, can have a simple analytical form [26]

$$F(j) \simeq 1 + \left(\frac{\sum_\sigma (|u_\sigma|^2 - |v_\sigma|^2)}{\sum_\sigma (|u_\sigma|^2 + |v_\sigma|^2)} \right)^2 = 1 + \delta_{\text{ph}}^2(j), \tag{4}$$

where $\delta_{\text{ph}}(j)$ denotes the local particle-hole asymmetry. Thus, the spatially resolved Fano factors can be used to identify the existence of MZM.

For the 2D SC, we use the Fu-Kane model for the superconducting topological surface states [5] which can be described by the BdG Hamiltonian (2), with its normal part being $\hat{h} = v_F(\boldsymbol{p} \times \boldsymbol{\sigma}) \cdot \boldsymbol{z} - \mu$, where v_F is the Fermi velocity of the surface Hamiltonian of a topological insulator and $\boldsymbol{p}$ represents the momentum operator [5]. The superconducting pair potential in this case is $\hat{\Delta} = \text{diag}(\Delta(\boldsymbol{r}), \Delta(\boldsymbol{r}))$ with the order parameter in real space being $\Delta(\boldsymbol{r}) = |\Delta(\boldsymbol{r})|e^{i\theta(\boldsymbol{r})}$, where $\theta(\boldsymbol{r})$ is the U(1) phase factor. In the presence of singly quantized vortices located at spatial positions $\{\boldsymbol{R}_j\}$ we may write

$$\theta(\boldsymbol{r}) = \sum_j \varphi_j(\boldsymbol{r}), \quad \varphi_j(\boldsymbol{r}) = \arg(\boldsymbol{r} - \boldsymbol{R}_j). \tag{5}$$

In addition $\Delta(\boldsymbol{r})$ vanishes at the center of each vortex and can be well approximated as $|\Delta(\boldsymbol{r})| \simeq \Delta_0 \prod_j \tanh(|\boldsymbol{r} - \boldsymbol{R}_j|/\xi)$. To perform tunneling calculations, we solve the continuous version of Hamiltonian (2) for the single vortex case directly in a disk with an open boundary condition [31–33].

The differential conductance of an MZM in a vortex core is presented in Fig. 1(b). For this continuous Fu-Kane model, we set $\{v_F/a,\ \Delta_0,\ \mu\} = \{2.0,\ 0.5,\ 0.25\}$ in unit of $\frac{\hbar v_F}{2a}$, leading to a BCS coherence length $\xi = \frac{v_F}{\Delta_0} = 4$. In the conductance calculation, we set the inverse temperature as $\beta = \frac{1\times10^4}{\Delta_0}$ and two different energy widths $\Gamma/\Delta_0 = 0.4,\ 0.1$. The quantized zero-bias conductance peak (ZBCP) is observed in the stronger tunneling condition, as shown in Fig. 1(b) with $\Gamma/\Delta_0 = 0.4$. These stringent requirements (extremely low temperature and strong tunneling condition) make it challenging to achieve the quantized conductance value in experimental setups and also lead to ambiguity in explaining the ZBCP.

Furthermore, based on Eq. (4), Fano factor tomography can be used to detect the presence of MZMs. Figure 1(c) illustrates the presence of a flat plateau of Fano factors near an isolated MZM (up to $r \sim \xi$), indicating its local particle-hole symmetric nature. Moving away from the core region, the Fano factors increase due to the decreased weight of the wave functions of bound states and the increasing significance of bulk states. In the region sufficiently distant from the vortex core, the dominance of Andreev reflections from the bulk states causes the Fano factor to reach 2. On the contrary, the spatially resolved Fano factors of trivial bound states exhibit strong oscillations between the values of 1 and 2 [34].

We summarize each Appendix here to close this section. Appendices A and E present simulations for the Caroli-de Gennes-Matricon (CdGM) bound states [35] and Yu-Shiba-Rusinov (YSR) bound states [36–38], respectively. We observe similar oscillations of the Fano factors in both cases. In Appendix C, we analyze the Majorana toy model proposed in Sec. III in detail to have a full understanding about the behavior of the measured Fano factors when tunneling into different bound states. In Appendix D, we use a 1D Majorana chain (a system consisting of many Majorana pairs) to examine the effect of the couplings between different individual Majorana pairs to the Fano factors measured in the high voltage regime. We calculate the tunneling characteristics of MZMs in a triangular vortex lattice in Appendix F. Finally, in Appendix B, we employ low-energy models to investigate the influence of the single-electron tunneling processes to the Fano factor tomography in order to explain the numerical results in Sec. IV. We further provide more simulations of the Fano factor tomography in the MZM vortex lattices at the end of Appendix B.

III. FANO FACTORS IN A MAJORANA TOY MODEL

After gaining the knowledge of a single MZM, we will focus on a pair of Majorana fermions and explore the physical picture behind Eq. (4) in this section. Since Dirac fermions can be expressed as a pair of Majorana fermions, we consider a trivial bound state as a pair of MBSs with finite overlap between their wave functions. Therefore we model the spatial overlap of the two Majorana wave functions as tunneling into these two MBSs simultaneously, with coupling amplitude w_0 and $\bar{w}e^{i\theta}$, respectively. The inset in Fig. 2(a) depicts our setup. Here, we choose a gauge that the coupling amplitude w_0 between the tip and the first MBS is purely real and the coupling with the second MBS can be a generic complex number
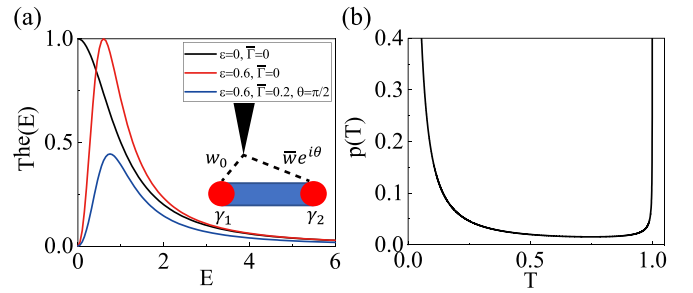

FIG. 2. (a) Schematic plot of the transmission eigenvalue at different cases where the inset depicts our toy model. Here we set the coupling between the tip and the MBS 1 as $\Gamma_0 = 1.0$. The black line depicts the case of tunneling into an isolated MZM, while in the red and blue lines we turn on the energy splitting between a pair of MBSs. In the blue line, we further turn on the coupling between the tip and MBS 2. (b) The distribution $p(T)$ for the case of tunneling only to one of a pair of Majorana fermions.

$\bar{w}e^{i\theta}$. By using scattering formalism [39], the transmission eigenvalue [40,41] at energy E can be expressed as [42]

$$T^{he}(E) = \frac{(\Gamma_0 + \bar{\Gamma})^2 - 4\Gamma_0\bar{\Gamma}\sin^2\theta}{\left(E - \frac{\varepsilon^2 + \Gamma_0\bar{\Gamma}\sin^2\theta}{E}\right)^2 + (\Gamma_0 + \bar{\Gamma})^2}, \qquad (6)$$

where $\Gamma_0 = 2\pi w_0^2$, $\bar{\Gamma} = 2\pi\bar{w}^2$, and ε is the energy splitting between these two MBSs. In this single channel tunneling problem, the time averaged current I and shot noise S in the zero-temperature limit, are

$$I = \frac{2e}{h}\int_0^{eV} dE\, T^{he}(E), \qquad (7)$$

$$S = \frac{8e^2}{h}\int_0^{eV} dE\, T^{he}(E)(1 - T^{he}(E)). \qquad (8)$$

In the Poisson limit where all the transmission eigenvalue $T^{he}(E) \ll 1$, the Fano factor defined in Eq. (3) represents the effective charge of the current carriers which in this case are the Cooper pairs. Under quantum transport conditions, the shot-noise due to the discrete nature of charge is weaker than its classical value since the transmitted electrons are correlated because of the Pauli principle [43,44]. From Eq. (6), we can observe that the maximum value of $T^{he}(E)$ is given by

$$\max(T^{he}(E)) = 1 - \frac{4\Gamma_0\bar{\Gamma}\sin^2\theta}{(\Gamma_0 + \bar{\Gamma})^2}, \qquad (9)$$

which can reach the perfect Andreev reflection peak only if $\bar{w}\sin\theta = 0$. In this case, the coupling matrix between the tip and these two MBSs are purely real, which is equivalent to coupling with only one of the MBSs.

Obtaining the general expression for the Fano factor with the transmission eigenvalue [Eq. (6)] at arbitrary voltage is hard. First, we examine the case of tunneling into an isolated MZM (i.e. $\varepsilon = 0$, $\bar{\Gamma} = 0$). In this case, the transmission eigenvalue simplifies to a Lorentz distribution given by $T^{he}(E) = \Gamma_0^2/(E^2 + \Gamma_0^2)$, making it easy to evaluate the integral in Eqs. (7) and (8). Consequently, the Fano factor is

[26,45]

$$F(V) = 1 - \frac{eV\Gamma_0}{\left[(eV)^2 + \Gamma_0^2\right]\arctan\left(\frac{eV}{\Gamma_0}\right)}. \quad (10)$$

In the high voltage limit ($eV \gg \Gamma_0$), the Fano factor approaches 1. The suppression of the Fano factor to half the Poisson limit can be attributed to the high transparency peak at $E = 0$ in T^{he}, as indicated by Eq. (8). When the tip tunnels into both MBSs and the tunneling matrix cannot be gauged into a purely real one, the transparency peak diminishes as $\bar{\Gamma}$ increasing (as long as $\bar{\Gamma} < \Gamma_0$), as shown in Fig. 2(a). This reduction alleviates the suppression in the quantum transport as described in Eq. (8), subsequently increasing the Fano factor. A finite energy splitting primarily shifts the peak of T^{he} [Eq. (6), and Fig. 2(a)], but it does not impact the Fano factor in the high voltage regime (details in Appendix C).

One can transform the uniform distribution in the energy interval [0, eV] in the integral (7) and (8) into the distribution of the transmission eigenvalue T. It turns out when tunneling into one of the two MBSs, the distribution $p(T) \propto \frac{1}{T^{3/2}\sqrt{1-T}}$ in the limit of $eV \gg \Gamma_i, \varepsilon$, as depicted in Fig. 2(b). The suppression of the shot noise below Poisson limit is a consequence of the bimodal distribution of transmission eigenvalues [46]. Instead of all Ts being close to the average transmission probability, the Ts are either close to 0 or to 1. This reduces the integral of $T(1 - T)$. The specific form of this bimodal distribution gives rise to the suppression factor 1/2. It is worth noted that the suppression 1/2 of the Fano factor not only occurs in tunneling to an isolated MZM but also happens in the symmetric double barrier junctions [43,47]. In the MZM case, the symmetric tunneling is guaranteed by the particle-hole symmetry of the Majorana wave function.

The distribution of transmission eigenvalues in a system with many pairs of Majorana fermions would typically deviate from the universal distribution $p(T)$ mentioned earlier. However, as discussed in Appendix D, if the couplings between these Majorana pairs are small compared to the tunneling energy width Γ, the Fano factor measured from the point contact measurement in the high voltage regime will still be almost 1.

IV. MZMS IN VORTEX LATTICES

Finally, we want to address the MZMs inside vortex lattices. It is well known that certain types of topological superconductors and superconducting topological surface states can host protected MZMs in the cores of Abrikosov vortices [3,5]. When these vortices are arranged in a dense periodic lattice, it is expected that the zero modes from neighboring vortices will hybridize and form dispersing bands [48–50]. This section primarily focuses on the square vortex lattice and examines the related properties of differential conductance and Fano factor tomography. The extension to other vortex lattices is straightforward. We discover that the conductance is significantly suppressed due to the couplings between MZMs located at different vortices, while Fano factor tomography can still be used to detect the existence of MZMs.

For a general MZM network, we can write down a general tight-binding Hamiltonian as

$$H_M = \frac{i}{2}\sum_{ij} t_{ij}\gamma_i\gamma_j, \quad (11)$$

where γ_i is a Majorana operator that satisfies $\gamma_i^\dagger = \gamma_i$ and $\{\gamma_i, \gamma_j\} = 2\delta_{ij}$. The point contact tunneling Hamiltonian between the normal tip and the SC can be described by

$$H_T = \sum_\sigma \int dx \, [\tilde{t}\delta(x)\psi_{T,\sigma}^\dagger(x)\psi_{S,\sigma}(x) + h.c.] \quad (12)$$

When $(eV, \Gamma) \ll \Delta$, the current is dominated by the low-lying Majorana states. Under Nambu representation, $\Psi = (\psi_\uparrow, \psi_\downarrow, \psi_\downarrow^\dagger, -\psi_\uparrow^\dagger)^T$, the projection of the field operator Ψ onto the Majorana states manifold can be approximated as $\Psi(x) \approx \sum_i \gamma_i[f_{\uparrow,i}(x), f_{\downarrow,i}(x), f_{\downarrow,i}^*(x), -f_{\uparrow,i}^*(x)]^T$. This approximation leads to the effective tunnel Hamiltonian that describes the coupling between the tip and the Majorana states as

$$H_T = \tilde{t}\sum_{\sigma,i}(\psi_{T,\sigma}^\dagger(0)f_{\sigma,i}(0) - \psi_{T,\sigma}(0)f_{\sigma,i}^*(0))\gamma_i. \quad (13)$$

In the practical case where the MZMs are well separated and the tip is located at a vortex core center, we can simplify the problem by considering a single Majorana bound state coupled to the tip. This can be achieved by defining the energy width matrix as $\tilde{\Gamma}_{ij} \equiv \delta_{i,0}\delta_{j,0}\tilde{\Gamma}$, where without loss of generality we denote this MBS as the zero-th MBS. Moreover, in the wide band limit, $\tilde{\Gamma}$ is energy independent and $\tilde{\Gamma} = 2\pi \nu_T \tilde{t}^2(|f_\uparrow|^2 + |f_\downarrow|^2)$, where f_σ is the zeroth Majorana wave function evaluated at the core center. In this scenario, at zero temperature, the differential conductance is given by [28]

$$G(V) = -\frac{2e^2}{h}\tilde{\Gamma}\text{Im}\big[G_{00}^R(eV)\big]. \quad (14)$$

Here, $G_{00}^R = g_{00}^R/(1 + i\tilde{\Gamma}g_{00}^R)$ and $g^R(\omega) = 2[\omega - 2it]^{-1}$ represents the free retarded Green function of the Majorana network.

Now we introduce the tight-binding Hamiltonian of the MZMs in the square vortex lattice. In order to properly account for the gauge field of the system, it is necessary to consider a two-vortex unit cell, as shown in Fig. 3(a). The Hamiltonian for this system can be written as [50]

$$H_\square = \frac{it}{2}\sum_R \gamma_R^A(\gamma_R^B - \gamma_{R-\hat{x}-\hat{y}}^B + \gamma_{R-\hat{x}}^B + \gamma_{R-\hat{y}}^B) + \text{H.c.}$$

$$+ \frac{it'}{2}\big[\gamma_R^A(-\gamma_{R+\hat{x}}^A + \gamma_{R+\hat{y}}^A) + \gamma_R^B(\gamma_{R+\hat{x}}^B - \gamma_{R+\hat{y}}^B)\big] + \text{H.c.}, \quad (15)$$

where the superscripts A and B denote two sublattices in the MZMs network and we have included nearest-neighbor (NN) and next nearest-neighbor (NNN) couplings. Figure 3(b) depicts a typical MZM band structure with a particle-hole symmetric bandwidth around $8\sqrt{2}t$. Figure 4 displays the corresponding zero-temperature differential conductance when the STM tip is located above one MZM. As shown in Fig. 4, compared to the isolated MZM case where the ZBCP is quantized at value of 2, the peak height of the tunneling differential
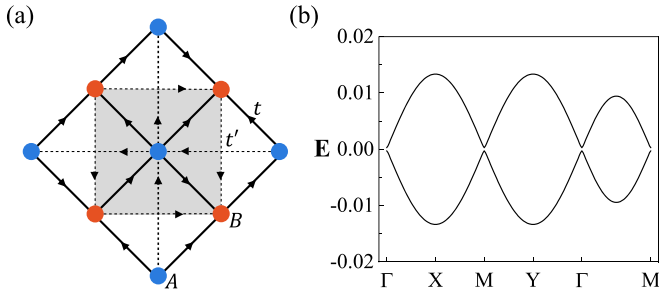
FIG. 3. (a) A diagrammatic sketch of a square vortex lattice with two vortices in one unit cell (the shaded region). Each vortex core binds an MZM, and the arrows specify the $\mathbb{Z}_2$ gauge factors for the MZM tight-binding models. Hopping in the direction of the arrow incurs a phase factor of $+i$ while hopping in the opposite direction $-i$. (b) A typical band structure when MZMs at different core sites hybridize to form a band. The values of t (NN hopping) and t' (NNN hopping) are $t = 2.36 \times 10^{-3}$ and $t' = 3.45 \times 10^{-5}$, respectively.

conductance of an MZM lattice is strongly suppressed to near one due to the coupling between MZMs, which vanishes outside the MZM band. This further complicates the explanation of the ZBCP which casts a shadow over the confirmation of the existence of MZM. However, as discussed above, we can gain insights of the MZM lattice from the Fano factor tomography introduced in Sec. II. In order to achieve a more accurate description of the vortex lattice, we use a periodic Hamiltonian for the Fu-Kane model in the presence of a vortex lattice. We take the vortex lattice approach proposed by Refs. [50,51] and perform the band calculation on a square lattice. The band structure for a square vortex lattice and a generic chemical potential μ is shown in Fig. 5(a). Besides the Majorana bands (red lines) around zero energy, there are bulk superconducting bands (black lines) with superconducting gaps. Tuning μ to the neutrality point ($\mu = 0$) results in the vanishing of couplings between the MZMs, leading to a completely flat Majorana band, which is shown in Fig. 5(b). This is because H_{FK} exhibits an extra chiral symmetry generated by $\Pi = \tau_z \sigma_z$ at the neutrality point. As an important
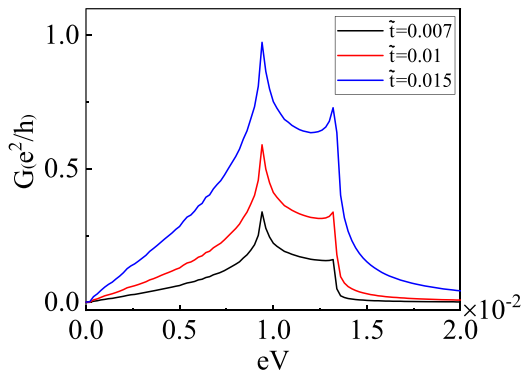

FIG. 4. The tunneling differential conductance of MZM networks at zero temperature. The parameters of the MZM network are the same as in the Fig. 3(b), and we set $\nu_T = 0.8$, $|f_\uparrow|^2 + |f_\downarrow|^2 = 1$ in the simulations. Under moderate tunneling strength, the conductance peak is significantly suppressed from the ideal quantized value of 2 when the hybridization is strong.
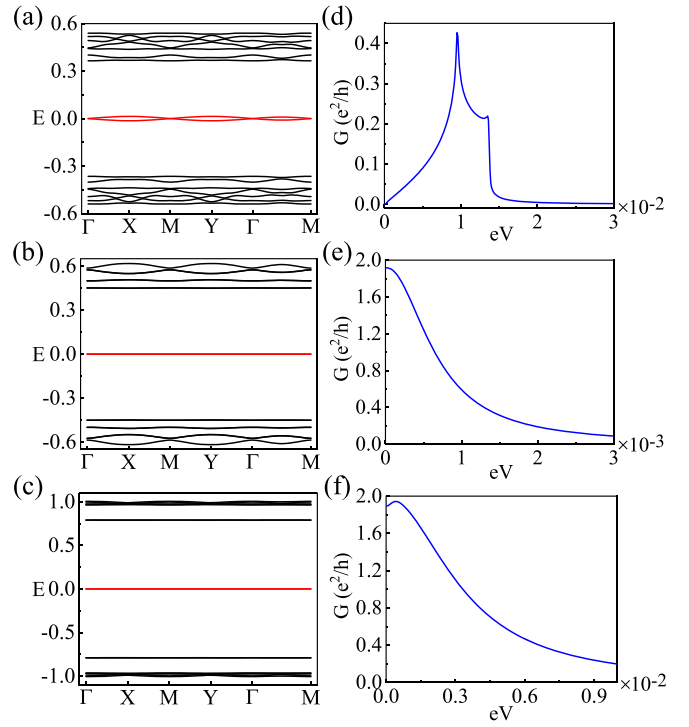

FIG. 5. (a)–(f) depict different cases of Majorana bands and their conductance at the vortex core center. The vortex lattice is constructed using a square lattice tight-binding model with a lattice constant of $a = 1$, where the nearest-neighbor hopping amplitude is set to $t = 1$. A 30×30 magnetic unit cell is considered for all cases. The energy width is set to $\Gamma = 0.16\Delta_0$, the inverse temperature is $\beta = 8000/\Delta_0$, and the relaxation parameter is $\eta = 1 \times 10^{-5}$. The other parameters used in the simulations are specified as follows: [(a) and (d)] $\{\mu, \Delta_0, \xi\} = \{0.25, 0.4, 1.2a\}$, [(b) and (e)] $\{0, 0.4, 1.2a\}$, [(c) and (f)] $\{0.25, 1.0, 3a\}$.

consequence, the overlap amplitudes $|t_{ij}|$ between distinct MZMs exactly vanish at this point [48]. Fig. 5(c) shows that a larger pairing amplitude Δ_0 results in a more localized MZM wave function and, consequently, smaller overlap amplitudes. Comparing Fig. 5(d) with Figs. 5(e) and 5(f), we observe that the differential conductance of an MZM in the vortex lattice can be substantially reduced, even though the Majorana band exhibits a weak dispersion.

Furthermore, we calculate the spatially resolved Fano factors of the Fu-Kane model in the presence of the vortex lattice. As shown in Figs. 6(a)–6(d), the Fano factors plateau at value of 1 near each vortex core, regardless of the tunneling parameter details (i.e., relaxation parameter η, tunneling energy width Γ and chemical potential μ of the Fu-Kane model). Away from the vortices, the occurrence of Andreev reflection from the bulk states is enhanced by a larger tunneling energy width Γ [as indicated by the blue lines in Figs. 6(a) and 6(c)]. When the wave functions of the MZMs from different vortex cores overlap, the Fano factor is expected to be greater than 1 in accordance with Eq. (4). However, Eq. (4) is valid only when the relaxation parameter, η, approaches zero, where the single electron tunneling process is suppressed and only the Andreev reflection remains. Since the MZM wave function is small in that region, the behavior of the Fano factor is highly
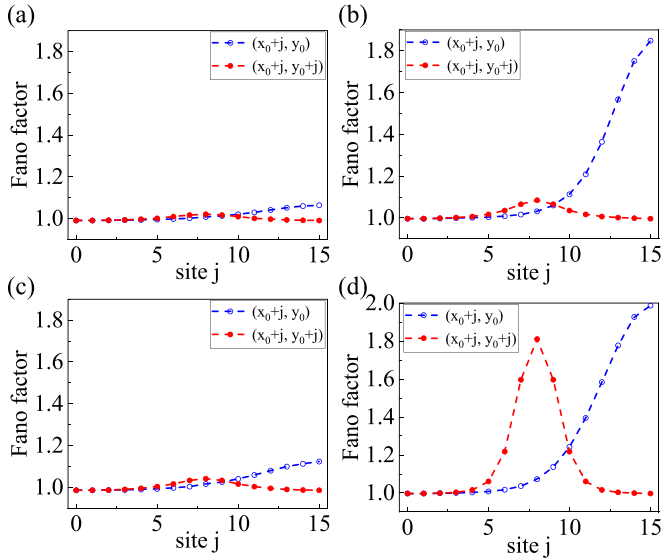
FIG. 6. (a)–(d) show the spatially resolved Fano factors near vortex cores and their dependence on tunneling parameters. The coordinate (x_0, y_0) represents the location of the vortex core center. In all cases, a pairing amplitude of $\Delta_0 = 0.4$ and a bias voltage $eV_{\text{bias}} = 0.15$ are used. The remaining parameters are specified as follows: (a) $\{\mu, \Gamma, \eta\} = \{0.25, 0.16\Delta_0, 1\times 10^{-5}\}$, (b) $\{0.25, 0.16\Delta_0, 1\times 10^{-11}\}$, (c) $\{0.25, 0.32\Delta_0, 1\times 10^{-5}\}$, and (d) $\{0, 0.16\Delta_0, 1\times 10^{-11}\}$. (a), (b), and (c) are corresponding to the case shown in Figs. 5(a) and 5(d), while (d) corresponds to Figs. 5(b) and 5(e). The values of the Fano factors plateau at 1 in the vicinity of a vortex core, regardless of the tunneling parameter details. As the relaxation parameter η approaches zero [cases (a) and (b)], and the energy width Γ increases [cases (a) and (c)], the effect of the overlapping between MZMs becomes more apparent (the red lines), and Andreev reflections from the bulk states begin to contribute to the Fano factors (the blue lines), away from the vortex core.

influenced by the finite relaxation parameter η. Additional cases of paired vortices and vortex lattices have been investigated in Appendix B. Spatially resolved Fano factors are less sensitive to the energy splitting of the Majorana bound states (or the dispersion of Majorana bands) compared to the differential conductance. Therefore, in cases where the overlap between the wave functions of the MZMs is not severe (but may still lead to a considerable energy splitting), Fano factor tomography may serve as a valuable tool to identify the existence of a well-separated MZM.

V. DISCUSSION

The technique of tunneling measurement is commonly employed for the identification of Majorana zero modes (MZMs). A characteristic feature of an isolated MZM is the presence of a quantized zero-bias conductance peak. However, due to factors like finite temperature, as well as couplings with other low-lying bound states, the observation of this quantization becomes exceedingly challenging in realistic experiments. In a previous study [26], the authors successfully demonstrated that current shot-noise spatial tomography with a metallic

tip can distinguish Majorana bound state from other trivial zero-energy fermionic states in 1D nanowires. In the high voltage regime, the Fano factors reflect the local particle-hole asymmetry of the bound state. Since the wave function of the MZM is local particle-hole symmetric, the Fano factor $F(j)$ near it will plateau at 1. In this paper, we point out that this suppression of the Fano factor to half of the Poisson limit is a consequence of the existence of a perfect transparency peak in the transmission eigenvalue $T^{he}(E)$. The finite energy splitting ε between these two MBSs primarily shifts the position of the transparency peak of $T^{he}(E)$ but has minimal effects on the Fano factor measured in the high voltage regime. When the wave functions of these two MBSs begin to overlap, both of the energy width Γ_0 and $\bar{\Gamma}$ become nonzero, which generally reduces the height of the transparency peak and increases the Fano factor in the high voltage regime. As $\bar{\Gamma}$ approaches Γ_0 and the phase angle $\theta \to \pi/2$, the Andreev reflection eigenvalue becomes vanishingly small and the Fano factor recovers its classical value of 2. We also note that tunneling into one MBS resembles tunneling through a symmetric double barrier junction. In fact, in the high voltage regime the distribution of the transmission eigenvalues is the same universal bimodal function which leads to a suppression factor $1/2$ in both cases.

In this paper, we apply the Fano factor tomography study to the 2D case. Our findings show that Fano factor tomography can effectively distinguish between MZM and CdGM bound states in the single vortex case. In the vicinity of an MZM, a flat plateau of $F = 1$ is observed, in stark contrast to the case of trivial in-gap states (such as CdGM bound states and YSR bound states), where strong spatial oscillations of F between values of 1 and 2 are obtained. In periodic vortex lattices, the MZMs within each vortex interact with each other, giving rise to a low-lying in-gap band. Our study demonstrates that, despite of the weak dispersion of the Majorana band, the differential conductance of an individual MZM can be significantly reduced. Conversely, the spatially resolved Fano factors exhibit lesser sensitivity to the energy splitting of the Majorana bound states and consistently plateau at 1 near each vortex core. As a result, Fano factor tomography can serve as an additional tool for identifying the presence of well-separated MZMs.

We further examine the influence of the single-electron tunneling processes on Fano factor tomography measurements. Single-electron tunneling can occur due to relaxation processes of in-gap bound states into the BCS continuum, which can be characterized by a finite relaxation parameter, η. It was found that the Fano factor can indicate local particle-hole asymmetry of bound states only when $\eta \ll \Gamma_j \ll eV$. An essential condition for this is a distinct separation between the density of states of in-gap states and bulk states. In experimental settings, temperature reduction can suppress relaxation from bound states to the quasiparticle continuum [52], thereby reducing η.

Recently, an ordered and tunable lattice of MZMs has been discovered in the iron pnictide compound LiFeAs [22]. Our results can facilitate the identification of isolated MZMs within the lattice and foster further experimental advancements of STM shot-noise experiments in the field of Majorana fermions.

APPENDIX A: CdGM BOUND STATES

For an ordinary s-wave superconductor, one can just replace $\hat{h}$ in Eq. (2) with $\hat{h} = \frac{p^2}{2m} - \mu$. Here we use a simplest square lattice model to simulate a 2D SC with a single vortex with the dispersion relation as $\hat{h} = -2t(\cos k_x + \cos k_y) + 4t - \mu$. The differential conductance and Fano factor tomography are presented in Fig. 7. At first sight of Fig. 7(a), one may feel strange about the vanishingly small conductance at the vortex core center. This is because we are working in the strong tunneling regime where the naive expectation that the differential conductance is proportional to the local density of states is no longer valid. In this case, it is the Andreev reflection that dominates in the tunneling current. For a SC with full spin rotation symmetry, the differential conductance near its in-gap bound states resonance can be given by

$$G(\omega) = \frac{2e^2}{h} \frac{8u^2v^2\Gamma^2\varepsilon^2}{[\omega^2 - (\varepsilon^2 - (u^2+v^2)^2\Gamma^2/4)]^2 + (u^2+v^2)^2\Gamma^2\varepsilon^2}, \quad \text{(A1)}$$

where ε is the energy of the lowest CdGM bound states. At the vortex core center, one of the u, v components of the CdGM bound states is zero [35], leading to a vanishingly small conductance.

Even though in this case the number of the lowest bound states are doubled due to the SU(2) degeneracy, the
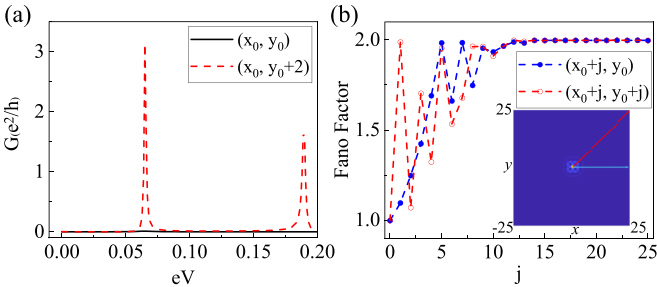

FIG. 7. Differential conductance and spatially resolved Fano factors are shown for a single vortex with CdGM bound states. The parameters in the simulation are $\{t, \mu, \Delta_0, \beta, \Gamma, \eta\} = \{1.5, 3.5, 0.8, 1\times10^4, 0.128, 1\times10^{-5}\}$. The inset in (b) shows the lowest lying eigenstate of the CdGM bound states, with arrows indicating the scanning directions. The vortex core is located at coordinates (x_0, y_0), and Fano factors were measured by setting a voltage bias of $eV_{\text{bias}} = 0.15$ between the energy of the lowest bound state and the second lowest state.

Fano factor tomography still has a strong spatial oscillation around the vortex core which is completely different with the MZM case.

APPENDIX B: FANO FACTORS OF A PAIR OF VORTICES AND VORTEX LATTICES

For a single-orbital Hamiltonian, a zero-energy bound state can be described by the Green's function, given by

$$g^R_{S;j,j}(\omega) = \frac{\phi_+(j)\phi_+^\dagger(j) + \phi_-(j)\phi_-^\dagger(j)}{\omega + i\eta}. \quad \text{(B1)}$$

Here, $\phi_+ = [u_\uparrow(j), u_\downarrow(j), v_\downarrow(j), -v_\uparrow(j)]^T$ represents the wave function associated with the zero-energy bound state, while $\phi_- = \tau_y\sigma_y\mathcal{K}\phi_+(j)$ is its particle-hole symmetric counterpart. Our primary focus is on the high-voltage regime, where $eV \gg \Gamma_j$, allowing us to consider $V \to \infty$. Additionally, we assume a temperature of $T = 0$. When the relaxation parameter $\eta \to 0^+$ and the Nambu-spinor ϕ_+ can be gauged into a real one, the integral of the current and the noise can be rigorously computed [26]. Consequently, the Fano factor is exact and given by Eq. (4). Remarkably, Eq. (4) remains accurate even for general complex Nambu-spinors, in agreement with previous findings [26].

Finite η, which physically could arise from the relaxation of the in-gap bound state to the BCS quasiparticle continuum, allows for single electron tunneling processes. In contrast to Andreev reflection, which transports Cooper pairs and has an effective charge of 2e, single-electron tunneling has an effective transport charge of 1e. Since the Fano factor reflects the effective transport charge (at least in the Poisson limit), single-electron tunneling can generally result in its reduction. Using Eq. (B1) as input, we can follow the calculation in Ref. [26] to obtain the Fano factor in the limit of $V \to \infty$. The full expression is cumbersome, so we will only consider two limits here. When $\eta \ll \Gamma_j$, Andreev reflection dominates, resulting in the Fano factor being

$$F \simeq 1 + \left(\frac{\sum_\sigma u_\sigma^2 - v_\sigma^2}{\sum_\sigma u_\sigma^2 + v_\sigma^2}\right)^2 \left(1 - A\frac{\eta}{\Gamma_j}\right) + O\left(\frac{\eta}{\Gamma_j}\right)^2, \quad \text{(B2)}$$

where the factor A is always positive and is given by

$$A = 4 + \frac{\left(\sum_\sigma u_\sigma^2 + v_\sigma^2\right)^2}{2\left(\sum_\sigma u_\sigma^2\right)\left(\sum_\sigma v_\sigma^2\right)}. \quad \text{(B3)}$$

As expected, a finite relaxation parameter η would lead to a reduction of the Fano factor from Eq. (4). In the reverse limit of $\eta \gg \Gamma_j$, the Fano factor is

$$F \simeq 1 - \left(\frac{\sum_\sigma u_\sigma^2 - v_\sigma^2}{\sum_\sigma u_\sigma^2 + v_\sigma^2}\right)^2 \frac{\Gamma_j}{\eta} + O\left(\frac{\Gamma_j}{\eta}\right)^2. \quad \text{(B4)}$$

In this case, single-electron tunneling dominates, and as $\eta \gg \Gamma_j$, the transmission transparency is low, resulting in $F \simeq 1$, which is the result of single-electron transport in the Poisson limit. As we can see, the Fano factor become featureless in this case. To ensure effective Fano factor tomography, we must operate in the regime where $\eta \ll \Gamma_j \ll eV$.

According to Eq. (B2), when the amplitudes of the wave function of bound states at site j are small (correspondingly,
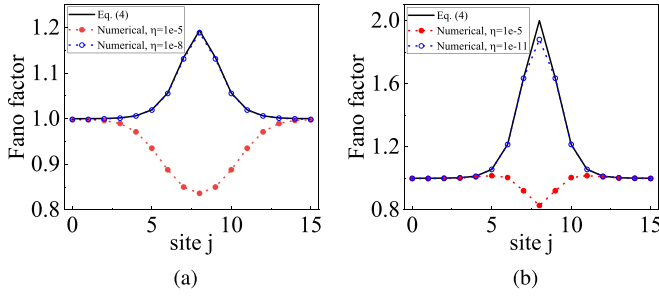
FIG. 8. This figure illustrates the spatially resolved Fano factors along the connected line of the two vortices in a Fu-Kane model. We use a square lattice to perform the numerical simulation, and the contribution is solely considered from the two MBSs. The figure displays the Fano factors for two different values of the chemical potential: (a) $\mu = 0.25$ and (b) 0. The solid lines represent the analytical results obtained from Eq. (4), while the data points correspond to the results of numerical simulations performed with varying relaxation parameter values η.

Γ_j would be small), the finite relaxation parameter will exert a significant influence on the Fano factor. Figure 8 illustrates the measured Fano factors of a Fu-Kane model with two vortices, obtained as the STM tip sweeps from one vortex to the other. To facilitate a direct comparison with Eq. (4), we neglected the contribution from the bulk states in the simulation. It can be observed from Figure 8 that when the tip is positioned near the mid-point between these two vortices, where the Majorana wave function is small, a significant deviation from the prediction of Eq. (4) arises due to the finite relaxation parameter, η. The numerical simulation coincides with the analytical prediction only when η is extremely small.

We calculated the Fano factor of the MZM vortex lattice under other parameters. As demonstrated in Fig. 9, the behavior of the spatially resolved Fano factors is similar with the results shown in the maintext. Near each vortex core, the Fano factors plateau at 1 regardless of the tunneling details. Away from the vortex core the Fano factor is sensitive to the relaxation parameter η and the energy width Γ as shown in Figs. 5 and 9. As the relaxation parameter η approaches zero, and the energy width Γ increases, the effect of the overlapping between MZMs starts to become apparent.

APPENDIX C: MAJORANA TOY MODEL AND SCATTERING METHOD

Here we provide a scattering scheme to understand the behavior of the Fano factors. We examine a pair of Majorana bound states (MBSs) using a single spinless electrode measurement setup. The Majorana Hamiltonian is given by $H_M = i\varepsilon\gamma_1\gamma_2$. The unitary scattering matrix $S(E)$ can be written as

$$S(E) \equiv \begin{pmatrix} s^{ee} & s^{eh} \\ s^{he} & s^{hh} \end{pmatrix}$$

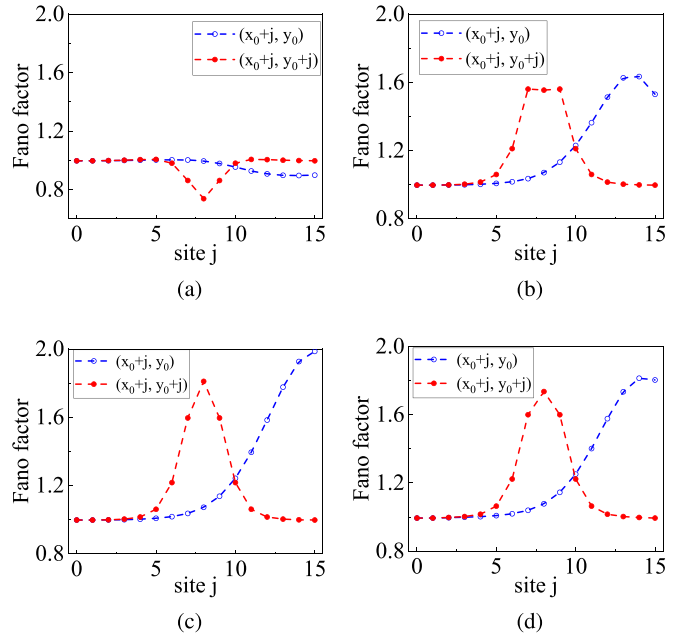$$= 1 + 2\pi i W^\dagger (H_M - E - i\pi WW^\dagger)^{-1} W, \quad \text{(C1)}$$

FIG. 9. These figures illustrate the spatially resolved Fano factors of a Fu-Kane model in the presence of a vortex lattice, with a fixed chemical potential of $\mu = 0$ under different tunneling parameters. The coordinate (x_0, y_0) represents the location of the vortex core center. In all cases, a pairing amplitude of $\Delta_0 = 0.4$ and a bias voltage $eV_{\text{bias}} = 0.15$ are used. The remaining parameters are specified as follows: (a) $\{\Gamma, \eta\} = \{0.16\Delta_0, 1 \times 10^{-5}\}$, (b) $\{0.16\Delta_0, 1 \times 10^{-9}\}$, (c) $\{0.16\Delta_0, 1 \times 10^{-11}\}$, and (d) $\{0.32\Delta_0, 1 \times 10^{-9}\}$.

with W the matrix that describes the coupling of the scatterer (Hamiltonian H_M) to the tip. In this toy model, we have

$$W = \begin{pmatrix} w_0 & w_0 \\ \bar{w}e^{i\theta} & \bar{w}e^{-i\theta} \end{pmatrix}, \quad H_M = \begin{pmatrix} 0 & i\varepsilon \\ -i\varepsilon & 0 \end{pmatrix}. \quad \text{(C2)}$$

The expression for H_M is in the basis $\{\Phi_1, \Phi_2\}$ of the two MBSs, while W is the coupling matrix in the basis $\{\Phi_e^{tip}, \Phi_h^{tip}\}$ of propagating electron and hole modes in the tip. We assume that the tip may couple to bound states 1 and 2 simultaneously due to the overlap of the two MBSs in real space. Without loss of generality, we can make w_0 purely real by adjusting the phase of the basis state in the tip.

The general expressions for the time averaged current $\bar{I}$ and shot noise S in the zero-temperature limit, in terms of the scattering matrix elements, are [39,53]

$$\bar{I} = \frac{e}{h} \int_0^{eV} dE(1 - T^{ee}(E) + T^{he}(E)), \quad \text{(C3)}$$

$$S = \frac{e^2}{h} \int_0^{eV} dE \mathcal{P}(E), \quad \text{(C4)}$$

with the definitions

$$\mathcal{P}(E) = T^{ee}(1 - T^{ee}) + T^{he}(1 - T^{he}) + 2T^{ee}T^{he}, \quad \text{(C5)}$$

$$T^{\alpha\beta}(E) = |s^{\alpha\beta}(E)|^2, \quad \alpha, \beta \in \{e, h\}. \quad \text{(C6)}$$

In this simple case, the unitary condition tells us that $T^{ee} + T^{he} \equiv 1$, and we can rewrite the current and the shot-noise in a more compact form,

$$\bar{I} = \frac{2e}{h} \int_0^{eV} dE \, T^{he}(E), \tag{C7}$$

$$S = \frac{8e^2}{h} \int_0^{eV} dE \, T^{he}(E)(1 - T^{he}(E)). \tag{C8}$$

Here $T^{he}(E)$ is exactly the transmission eigenvalue with $T^{he}(E) \in [0, 1]$. For a trivial NS junction, in the zero-temperature, zero voltage limit, the shot-noise is given by [40]

$$S_{NS} = 8e|V|\frac{e^2}{h} \sum_n T_n^{he}(1 - T_n^{he}), \tag{C9}$$

and the current $I = G_{NS}V = \frac{2e^2 V}{h} \sum_n T_n^{he}$. These transmission eigenvalues are all evaluated at $E = 0$. Usually for a trivial NS junction, all these eigenvalues are small (i.e., in the so-called Poisson limit of transport), and the Fano factor $F = 2$ is exactly the effective charge of the current carriers (Cooper pair transport). In our case, when we tunnel into a strictly isolated MZM (i.e., when the energy splitting $\varepsilon = 0$ and $\bar{w} = 0$), the particle-hole symmetry together with the requirements from the topologically non-trivial case enforce the transmission eigenvalue $T^{he}(E = 0) = 1$ (perfect Andreev reflection). In this case, the Fano factor will vanish in the zero voltage limit [45,54]. However, Majorana fermions always come in pairs, and there are inevitable couplings and finite energy splittings between these Majorana fermions, which would bring the Fano factor back to a value of 2 in the limit of $eV \ll \varepsilon$ [45], yielding the same result as the trivial NS junction. Therefore it is challenging to identify the existence of MZM through measuring the Fano factor in the zero-voltage limit.

By substituting Eq. (C1) for the pair of MBSs, we can derive the expression for the transmission eigenvalue:

$$T^{he}(E) = \frac{(\Gamma_0 + \bar{\Gamma})^2 - 4\Gamma_0\bar{\Gamma}\sin^2\theta}{\left(E - \frac{\varepsilon^2 + \Gamma_0\bar{\Gamma}\sin^2\theta}{E}\right)^2 + (\Gamma_0 + \bar{\Gamma})^2}, \tag{C10}$$

where $\Gamma_0 = 2\pi w_0^2$ and $\bar{\Gamma} = 2\pi\bar{w}^2$.

In the limit of $eV \gg \Gamma, \varepsilon$, we can prove that a finite energy splitting ε does not affect the Fano factor, by noting the fact that the following integrals are independent of the energy shift λ.

$$\int_0^\infty dE \, T(E), \quad \int_0^\infty dE \, T^2(E), \quad \text{where}$$

$$T(E) = \frac{\Gamma^2}{\left(E - \frac{\lambda^2}{E}\right)^2 + \Gamma^2}. \tag{C11}$$

Considering that

$$\partial_\lambda T(E)$$

$$= 4\lambda\Gamma^2 \left[\frac{1}{\left(\left(E - \frac{\lambda^2}{E}\right)^2 + \Gamma^2\right)^2} - \frac{\lambda^2/E^2}{\left(\left(E - \frac{\lambda^2}{E}\right)^2 + \Gamma^2\right)^2} \right], \tag{C12}$$

the integral of $\partial_\lambda T(E)$ from zero to infinity vanishes since we can apply a change of variables of $E \to \lambda^2/E$ to the first term

and can immediately observe the integrals of these two terms cancel exactly. For a similar reason, the integral of $T^2(E)$ is also independent of λ. Therefore we can evaluate the integral in Eq. (C11) at $\lambda = 0$, and they turn out to be

$$\int_0^\infty dE \, T(E) = \frac{\pi}{2}\Gamma,$$

$$\int_0^\infty dE \, T^2(E) = \frac{\pi}{4}\Gamma. \tag{C13}$$

With these results in hand, the Fano factor has a simple form in the high voltage limit, given by

$$F \equiv \frac{S}{2e\bar{I}} = 1 + \frac{2\Gamma_0\bar{\Gamma}(1 - \cos 2\theta)}{(\Gamma_0 + \bar{\Gamma})^2}. \tag{C14}$$

This suggests that in the high voltage regime, the Fano factor is insensitive to the energy splitting between the two MZMs. When their wave functions overlap (i.e. $\bar{w}\sin\theta \neq 0$), the Fano factor will be greater than 1.

We can also establish a connection between this Majorana toy model and the case of tunneling into a spin-polarized in-gap bound state. We start from a general tunneling Hamiltonian

$$H_{\text{tunnel}} = \frac{t}{2}[\psi_T^\dagger \tau_z \psi_S(j) + \text{H.c.}], \tag{C15}$$

where ψ_T and $\psi_S(j)$ correspond to the Nambu spinors of the normal tip and the superconductor at site j, respectively, given by $\psi_T = (d_\uparrow, d_\downarrow, d_\downarrow^\dagger, -d_\uparrow^\dagger)^T$ and $\psi_S(j) = (c_{\uparrow,j}, c_{\downarrow,j}, c_{\downarrow,j}^\dagger, -c_{\uparrow,j}^\dagger)^T$. By projecting $\psi_S(j)$ onto the low energy bound states manifold,

$$\psi_S(j) \simeq \sum_{\pm 1} \phi_{\pm 1}(j)\alpha_{\pm 1}, \quad \alpha_n = \sum_j \phi_n^\dagger(j)\psi_S(j), \tag{C16}$$

where ϕ_n is the orthonormal eigenstate of the BdG Hamiltonian of the SC which satisfies the relation $\phi_{-n}(j) = \tau_y\sigma_y\mathcal{K}\phi_{+n}(j)$ because of the particle-hole symmetry. The fermionic operator α_n obeys the standard anti-commutation relations, and it holds that $\alpha_{+n}^\dagger = \alpha_{-n}$. Denoting the wave functions of the in-gap bound states as $\phi_{+1}(j) = (u_\uparrow, u_\downarrow, v_\downarrow, -v_\uparrow)^T$ and $\phi_{-1}(j) = \tau_y\sigma_y\mathcal{K}\phi_{+1}(j)$, we can approximate the tunneling Hamiltonian as

$$H_{\text{tunnel}} = t[(u_\uparrow d_\uparrow^\dagger + u_\downarrow d_\downarrow^\dagger)\alpha_{+1} + (v_\uparrow^* d_\uparrow^\dagger + v_\downarrow^* d_\downarrow^\dagger)\alpha_{-1}] + \text{H.c.} \tag{C17}$$

We consider the case where the spins are polarized, specifically $u_\downarrow$ and $v_\downarrow$ are equal to zero. Using $\alpha_{+1}^\dagger = \alpha_{-1}$, we can define two Majorana operators: $\gamma_1 = \alpha_{+1} + \alpha_{+1}^\dagger$, $\gamma_2 = -i(\alpha_{+1} - \alpha_{+1}^\dagger)$. This allows us to simplify the tunneling Hamiltonian (C17) as follows:

$$H_{\text{tunnel}} = \frac{t}{2}[(u_\uparrow + v_\uparrow^*)d_\uparrow^\dagger\gamma_1 + i(u_\uparrow - v_\uparrow^*)d_\uparrow^\dagger\gamma_2] + \text{H.c.} \tag{C18}$$

After a gauge transformation to ensure that the coupling with Majorana 1 is real, we can directly apply Eq. (C14). Consequently, in the high voltage regime, the Fano factor can be
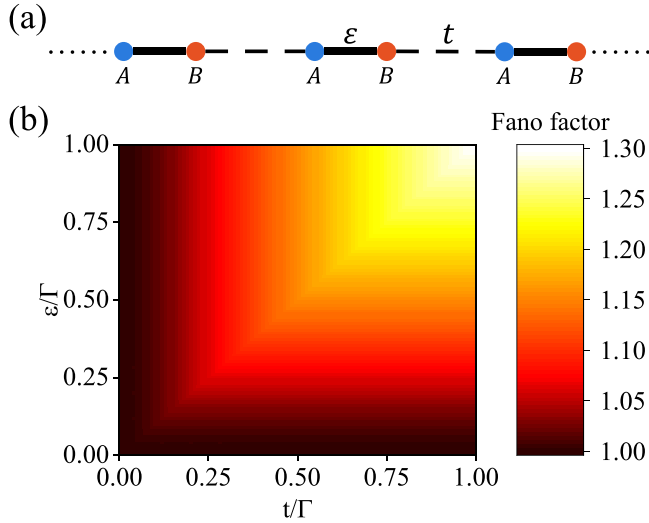
FIG. 10. (a) A diagrammatic sketch of a 1D Majorana chain. (b) Point contact measured Fano factors in the limit of $eV \to \infty$.

expressed as

$$F = 1 + \left(\frac{|u_\uparrow|^2 - |v_\uparrow|^2}{|u_\uparrow|^2 + |v_\uparrow|^2} \right)^2, \quad \text{(C19)}$$

which reflects the local particle-hole asymmetry of the in-gap bound state, as stated by Eq. (4) in the main text.

APPENDIX D: 1D MAJORANA CHAIN

In order to include the effect of couplings between many Majorana pairs, we consider a simple 1D Majorana tight binding model:

$$H = \sum_j \frac{i\varepsilon}{2} \gamma_{B,j} \gamma_{A,j} + \frac{it}{2} \gamma_{A,j+1} \gamma_{B,j} + \text{H.c.} \quad \text{(D1)}$$

As indicated in Fig. 10(a), ε is the energy splitting of each individual Majorana pair and t represents the hybridizing between these pairs. For $\varepsilon = t$, it is a homogeneous infinite Majorana chain, while when $\varepsilon \gg t$, it is decoupled into many independent Majorana pairs. In the case of point contact measurement, the current and shot-noise still have the form of Eqs. (7) and (8). The transmission eigenvalue can be calculated by Eq. (14), which is given by $T(\omega) = -\Gamma \text{Im} G_{00}^R(\omega)$.

We calculate its saturate Fano factor in the $eV \to \infty$ limit. As depicted in Fig. 10(b), for a fixed hybridizing strength t, in the region of $\varepsilon > t$ (otherwise the energy splitting of each Majorana pair should be interpreted as t rather than ε), Fano factor in the high voltage regime is not sensitive to the energy splitting ε inside an MBS pair. When these Majorana pairs begin to hybridize, the Fano factor increasingly deviates from 1 as t increasing. For $t \lesssim 0.2\Gamma$, the observation of the Fano factors in a single pair of MBSs is still valid in the chain model.

We further choose several parameters and calculate the transmission eigenvalue $T(\omega)$ and the corresponding distribution $p(T)$. Figures 11(a) and 11(b) show the transmission eigenvalue $T(\omega)$ for two sets of parameters, and the corresponding Fano factors measured in the high voltage limit are
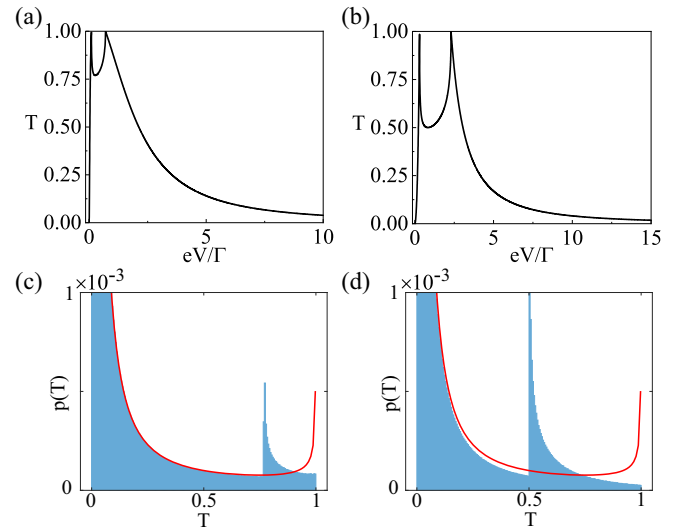

FIG. 11. (a)–(d) Transmission eigenvalues $T(\omega)$ at different ε, t parameters and their corresponding distributions $p(T)$. [(a) and (c)] $\varepsilon = 0.2\Gamma$, $t = 0.15\Gamma$, [(b) and (d)] $\varepsilon = 0.65\Gamma$, $t = 0.5\Gamma$. The red line indicates the distribution $p(T) \propto \frac{1}{T^{3/2}\sqrt{1-T}}$.

$F = 1.03$ and 1.15, respectively. However, as demonstrated in Figs. 11(c) and 11(d), the distribution $p(T)$ deviates from the universal distribution mentioned in the main text in both cases. It turns out that $p(T)$ may be hard to characterize $F(\infty)$ quantitatively in a system consisting of many Majorana pairs.

APPENDIX E: YSR BOUND STATES

We also analyze the case of Yu-Shiba-Rusinov (YSR) states in our study. For a single magnetic impurity, we consider the BdG Hamiltonian,

$$H = H_0 + H_{\text{imp}} = \xi_k \tau_3 \sigma_0 + \Delta \tau_1 \sigma_0 + J S_z \tau_0 \sigma_3 \delta(\boldsymbol{r}). \quad \text{(E1)}$$
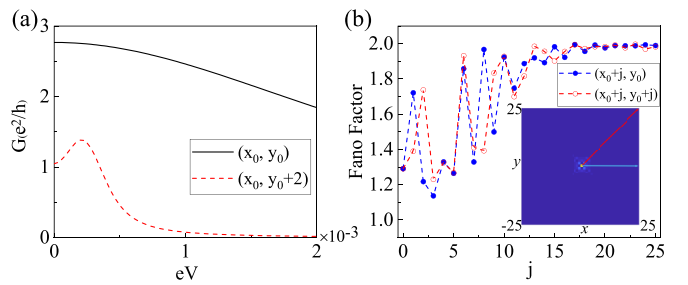

FIG. 12. (a) Differential conductance of a YSR bound state. (b) Spatially resolved Fano factors in the 2D plane. The coordinate (x_0, y_0) represents the location of the magnetic impurity. The simulation was performed using a 2D square lattice tight-binding model with nearest-neighbor hopping strength $t_1 = -1.5$ and a chemical potential $\mu = 3.5$, measured from the bottom of the band. A pairing field of $\Delta = 0.4$ and an exchange strength of $JS_z = 3.45$ were set to induce a deep YSR bound state. In the tunneling simulations, an energy width of $\Gamma = 0.1\Delta$, a relaxation parameter of $\eta = 1 \times 10^{-5}$ and an inverse temperature of $\beta = 8000/\Delta$ were used. For the Fano factor simulation (b), a fixed voltage bias of $eV_{\text{bias}} = 0.2$ is applied.
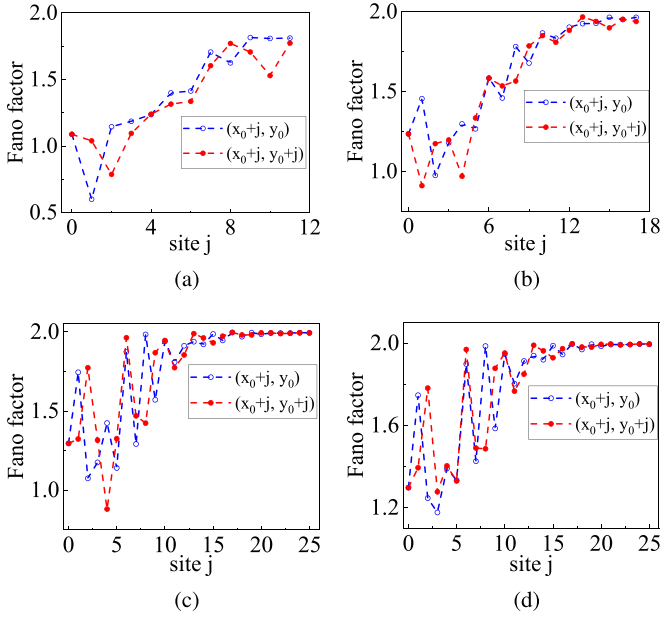
FIG. 13. Fano factor tomography of magnetic impurity lattices with different distances d between impurities is presented. The distances are specified as (a) $d = 23a$, (b) $35a$, (c) $51a$, and (d) $75a$, where a represents the lattice constant of the tight-binding model introduced earlier. The coordinates of one of the magnetic impurities are denoted as (x_0, y_0). In the simulations, we maintain a fixed applied voltage of $eV_{\text{bias}} = 0.25$, while all other parameters remain the same as in Fig. 12.

Here, we assume the impurity potential is purely local, with the impurity spin S pointing along the z direction. In the wide band limit, the energy of the bound state is given by [38,55] $\varepsilon = \Delta \cos(2\delta_0)$, where $\tan \delta_0 = \pi \nu_0 J S_z$ and ν_0 represents the normal state density of states at the Fermi level. The bound state wave functions at the impurity location are [10,56]

$$\phi_+(0) = \frac{1}{\sqrt{\mathcal{N}}}\begin{pmatrix} 1 \\ 0 \\ -1 \\ 0 \end{pmatrix}, \quad \phi_-(0) = \frac{1}{\sqrt{\mathcal{N}}}\begin{pmatrix} 0 \\ 1 \\ 0 \\ 1 \end{pmatrix}. \quad \text{(E2)}$$

The behavior of the wave function away from the impurity depends strongly on the dimensionality of the system. In three dimensions (3D), the wave function decays as $\frac{1}{r}\exp(-r\sqrt{\Delta^2 - \varepsilon^2}/\hbar v_F)$. However, in two dimensions (2D), it decays much slower, going as [56] $\frac{1}{\sqrt{r}}\exp(-r\sqrt{\Delta^2 - \varepsilon^2}/\hbar v_F)$. Here, we focus on the 2D case, where the wave function away from the impurity can be expressed as

$$\phi_+(r) = \frac{1}{\sqrt{\mathcal{N}\pi k_F r}}\begin{pmatrix} \sin\left(k_F r - \frac{\pi}{4} + \delta_0\right) \\ 0 \\ -\sin\left(k_F r - \frac{\pi}{4} - \delta_0\right) \\ 0 \end{pmatrix}$$

$$\times \exp\left(-\frac{\sqrt{\Delta^2 - \varepsilon^2}}{\hbar v_F}r\right), \quad \text{(E3)}$$

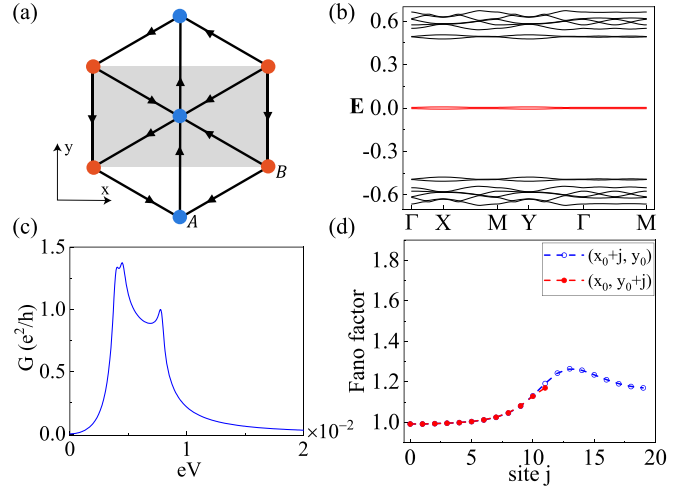

FIG. 14. (a) Example of A and B sublattices for the triangular vortex lattice. (b) The band structure of a triangular vortex lattice with a 38×22 magnetic unit cell. The parameters are $\{\mu, \Delta_0, \xi\} = \{0.18, 0.5, 1.2a\}$. (c) The differential conductance at the center of a vortex core. (d) The spatially resolved Fano factors near vortex cores, where the coordinate (x_0, y_0) represents the location of a vortex core center. In the calculations, the energy width is set to $\Gamma = 0.32\Delta_0$, the inverse temperature is $\beta = 8000/\Delta_0$, and the relaxation parameter is $\eta = 1 \times 10^{-5}$. In the simulations of the Fano factor tomography, the bias voltage is fixed at $eV_{\text{bias}} = 0.25$.

where $\mathcal{N}$ is a normalization factor and $\phi_-(r) = \tau_y \sigma_y \mathcal{K} \phi_+(r)$. Clearly, the YSR bound state exhibits spatially oscillating electron-hole asymmetry, which can potentially be characterized through Fano factor tomography. In the case of deep YSR states, corresponding to a dephasing $2\delta_0 \to \pm\pi/2$, the electron and hole YSR density of states exhibit antiphase behavior far from the impurity. This antiphase behavior leads to a strong spatial oscillation of the Fano factor as outlined in Eq. (4). The Appendix Fig. 12 demonstrates the differential conductance and the spatially resolved Fano factors of a deep YSR state. The deep YSR state exhibits a ZBCP signature, although it is not quantized. The Fano factor tomography of the deep YSR state strongly oscillates near the magnetic impurity and saturates at a value of 2 due to the dominant contribution of Andreev reflections from bulk states.

We also perform Fano factor tomography calculations in the presence of multiple magnetic impurities. To simplify the calculations, we assume that the magnetic impurities have the same exchange strength $J S_z$ and are periodically arranged into a square lattice. The numerical results demonstrate that as long as the impurity lattice is not too dense, the Fano factor tomography remains effective in capturing the signature of spatially oscillating electron-hole asymmetry in the YSR bound states, as shown in Fig. 13. However, as the impurities become denser, the Fano factors near a magnetic impurity decrease. This reduction can be attributed to the increased occurrence of single-electron tunneling processes. Specifically, as the impurities get closer, the overlaps between their respective bound states become more pronounced, leading to an increase in the effective single-electron tunneling channels and contributing to the single-electron tunneling current.

APPENDIX F: TRIANGULAR VORTEX LATTICE

In this Appendix, we perform calculations of tunneling characteristics on a triangular vortex lattice. As is shown in Fig. 14, the (local) tunneling characteristics of a square vortex lattice and a triangular vortex lattice are very similar. In both cases, the differential conductance shows a suppression due to the couplings between the MZMs. More over, the MZM in a triangular vortex lattice also has a smooth Fano factor plateau with a value of 1 near the vortex core. These results demonstrate that our conclusion in Sec. IV is very general and will also apply to the triangular vortex lattices.

[1] C. Nayak, S. H. Simon, A. Stern, M. Freedman, and S. Das Sarma, Non-abelian anyons and topological quantum computation, Rev. Mod. Phys. **80**, 1083 (2008).

[2] A. Y. Kitaev, Unpaired Majorana fermions in quantum wires, Phys. Usp. **44**, 131 (2001).

[3] N. Read and D. Green, Paired states of fermions in two dimensions with breaking of parity and time-reversal symmetries and the fractional quantum hall effect, Phys. Rev. B **61**, 10267 (2000).

[4] J. Alicea, New directions in the pursuit of Majorana fermions in solid state systems, Rep. Prog. Phys. **75**, 076501 (2012).

[5] L. Fu and C. L. Kane, Superconducting proximity effect and Majorana fermions at the surface of a topological insulator, Phys. Rev. Lett. **100**, 096407 (2008).

[6] R. M. Lutchyn, J. D. Sau, and S. Das Sarma, Majorana fermions and a topological phase transition in semiconductor-superconductor heterostructures, Phys. Rev. Lett. **105**, 077001 (2010).

[7] Y. Oreg, G. Refael, and F. von Oppen, Helical liquids and Majorana bound states in quantum wires, Phys. Rev. Lett. **105**, 177002 (2010).

[8] R. M. Lutchyn, E. P. A. M. Bakkers, L. P. Kouwenhoven, P. Krogstrup, C. M. Marcus, and Y. Oreg, Majorana zero modes in superconductor–semiconductor heterostructures, Nat. Rev. Mater. **3**, 52 (2018).

[9] S. Nadj-Perge, I. K. Drozdov, B. A. Bernevig, and A. Yazdani, Proposal for realizing Majorana fermions in chains of magnetic atoms on a superconductor, Phys. Rev. B **88**, 020407(R) (2013).

[10] F. Pientka, L. I. Glazman, and F. von Oppen, Topological superconducting phase in helical shiba chains, Phys. Rev. B **88**, 155420 (2013).

[11] F. Pientka, A. Keselman, E. Berg, A. Yacoby, A. Stern, and B. I. Halperin, Topological superconductivity in a planar Josephson junction, Phys. Rev. X **7**, 021032 (2017).

[12] M. Hell, M. Leijnse, and K. Flensberg, Two-dimensional platform for networks of Majorana bound states, Phys. Rev. Lett. **118**, 107701 (2017).

[13] H. Ren, F. Pientka, S. Hart, A. T. Pierce, M. Kosowsky, L. Lunczer, R. Schlereth, B. Scharf, E. M. Hankiewicz, L. W. Molenkamp, B. I. Halperin, and A. Yacoby, Topological superconductivity in a phase-controlled Josephson junction, Nature (London) **569**, 93 (2019).

[14] A. Fornieri, A. M. Whiticar, F. Setiawan, E. Portolés, A. C. C. Drachmann, A. Keselman, S. Gronin, C. Thomas, T. Wang, R. Kallaher, G. C. Gardner, E. Berg, M. J. Manfra, A. Stern, C. M. Marcus, and F. Nichele, Evidence of topological superconductivity in planar Josephson junctions, Nature (London) **569**, 89 (2019).

[15] O. Lesser, Y. Oreg, and A. Stern, One-dimensional topological superconductivity based entirely on phase control, Phys. Rev. B **106**, L241405 (2022).

[16] Y.-M. Xie, E. Lantagne-Hurtubise, A. F. Young, S. Nadj-Perge, and J. Alicea, Gate-defined topological Josephson junctions in bernal bilayer graphene, Phys. Rev. Lett. **131**, 146601 (2023).

[17] N. Hao and J. Hu, Topological quantum states of matter in iron-based superconductors: from concept to material realization, Natl. Sci. Rev. **6**, 213 (2019).

[18] Z. Wang, P. Zhang, G. Xu, L. K. Zeng, H. Miao, X. Xu, T. Qian, H. Weng, P. Richard, A. V. Fedorov, H. Ding, X. Dai, and Z. Fang, Topological nature of the $FeSe_{0.5}Te_{0.5}$ superconductor, Phys. Rev. B **92**, 115119 (2015).

[19] X. Wu, S. Qin, Y. Liang, H. Fan, and J. Hu, Topological characters in $Fe(Te_{1-x}Se_x)$ thin films, Phys. Rev. B **93**, 115129 (2016).

[20] G. Xu, B. Lian, P. Tang, X.-L. Qi, and S.-C. Zhang, Topological superconductivity on the surface of Fe-based superconductors, Phys. Rev. Lett. **117**, 047001 (2016).

[21] D. Wang, L. Kong, P. Fan, H. Chen, S. Zhu, W. Liu, L. Cao, Y. Sun, S. Du, J. Schneeloch, R. Zhong, G. Gu, L. Fu, H. Ding, and H.-J. Gao, Evidence for Majorana bound states in an iron-based superconductor, Science **362**, 333 (2018).

[22] M. Li, G. Li, L. Cao, X. Zhou, X. Wang, C. Jin, C.-K. Chiu, S. J. Pennycook, Z. Wang, and H.-J. Gao, Ordered and tunable Majorana-zero-mode lattice in naturally strained lifeas, Nature (London) **606**, 890 (2022).

[23] F. Massee, Q. Dong, A. Cavanna, Y. Jin, and M. Aprili, Atomic scale shot-noise using cryogenic MHz circuitry, Rev. Sci. Instrum. **89**, 093708 (2018).

[24] K. M. Bastiaans, T. Benschop, D. Chatzopoulos, D. Cho, Q. Dong, Y. Jin, and M. P. Allan, Amplifier for scanning tunneling microscopy at MHz frequencies, Rev. Sci. Instrum. **89**, 093709 (2018).

[25] K. M. Bastiaans, D. Chatzopoulos, J.-F. Ge, D. Cho, W. O. Tromp, J. M. van Ruitenbeek, M. H. Fischer, P. J. de Visser, D. J. Thoen, E. F. C. Driessen, T. M. Klapwijk, and M. P. Allan, Direct evidence for cooper pairing without a spectral gap in a disordered superconductor above T_c, Science **374**, 608 (2021).

[26] V. Perrin, M. Civelli, and P. Simon, Identifying Majorana bound states by tunneling shot-noise tomography, Phys. Rev. B **104**, L121406 (2021).

[27] K. T. Law, P. A. Lee, and T. K. Ng, Majorana fermion induced resonant andreev reflection, Phys. Rev. Lett. **103**, 237001 (2009).

[28] K. Flensberg, Tunneling characteristics of a chain of Majorana bound states, Phys. Rev. B **82**, 180516(R) (2010).

[29] S. Zhu, L. Kong, L. Cao, H. Chen, M. Papaj, S. Du, Y. Xing, W. Liu, D. Wang, C. Shen, F. Yang, J. Schneeloch, R. Zhong, G. Gu, L. Fu, Y.-Y. Zhang, H. Ding, and H.-J. Gao,

Nearly quantized conductance plateau of vortex zero mode in an iron-based superconductor, Science **367**, 189 (2020).

[30] G. Stefanucci and R. van Leeuwen, *Nonequilibrium Many-Body Theory of Quantum Systems: A Modern Introduction* (Cambridge University Press, Cambridge, 2013).

[31] J.-X. Zhu, *Bogoliubov-de Gennes Method and Its Applications* (Springer International Publishing, Switzerland, 2016).

[32] F. Gygi and M. Schlüter, Self-consistent electronic structure of a vortex line in a type-II superconductor, Phys. Rev. B **43**, 7609 (1991).

[33] L. Mao and C. Zhang, Robustness of Majorana modes and minigaps in a spin-orbit-coupled semiconductor-superconductor heterostructure, Phys. Rev. B **82**, 174506 (2010).

[34] Examples of CdGM bound states and YSR bound states are presented in Appendix A and E, respectively.

[35] C. Caroli, P. De Gennes, and J. Matricon, Bound fermion states on a vortex line in a type II superconductor, Phys. Lett. **9**, 307 (1964).

[36] Yu. Luh, Bound state in superconductors with paramagnetic impurities, Acta Phys. Sin. **21**, 75 (1965).

[37] H. Shiba, Classical spins in superconductors, Prog. Theor. Phys. **40**, 435 (1968).

[38] A. I. Rusinov, Superconductivity near a paramagnetic impurity, JETP Lett. **9**, 146 (1969).

[39] J. Nilsson, A. R. Akhmerov, and C. W. J. Beenakker, Splitting of a cooper pair by a pair of Majorana bound states, Phys. Rev. Lett. **101**, 120403 (2008).

[40] M. J. M. de Jong and C. W. J. Beenakker, Doubled shot noise in disordered normal-metal–superconductor junctions, Phys. Rev. B **49**, 16070 (1994).

[41] S. M. Girvin and K. Yang, *Modern Condensed Matter Physics* (Cambridge University Press, Cambridge, 2019).

[42] The derivation can be seen in the Appendix C.

[43] M. J. M. de Jong and C. W. J. Beenakker, Shot noise in mesoscopic systems, in *Mesoscopic Electron Transport*, edited by L. L. Sohn, L. P. Kouwenhoven, and G. Schön (Springer Netherlands, Dordrecht, 1997), pp. 225–258.

[44] L. S. Levitov and G. B. Lesovik, Charge distribution in quantum shot noise, J. Exp. Theor. Phys. Lett. **58**, 230 (1993).

[45] A. Golub and B. Horovitz, Shot noise in a Majorana fermion chain, Phys. Rev. B **83**, 153415 (2011).

[46] C. W. J. Beenakker and M. Büttiker, Suppression of shot noise in metallic diffusive conductors, Phys. Rev. B **46**, 1889 (1992).

[47] L. Y. Chen and C. S. Ting, Theoretical investigation of noise characteristics of double-barrier resonant-tunneling systems, Phys. Rev. B **43**, 4534 (1991).

[48] M. Cheng, R. M. Lutchyn, V. Galitski, and S. Das Sarma, Tunneling of anyonic Majorana excitations in topological superconductors, Phys. Rev. B **82**, 094504 (2010).

[49] R. R. Biswas, Majorana fermions in vortex lattices, Phys. Rev. Lett. **111**, 136401 (2013).

[50] T. Liu and M. Franz, Electronic structure of topological superconductors in the presence of a vortex lattice, Phys. Rev. B **92**, 134519 (2015).

[51] O. Vafek, A. Melikyan, M. Franz, and Z. Tešanović, Quasiparticles and vortices in unconventional superconductors, Phys. Rev. B **63**, 134509 (2001).

[52] M. Ruby, F. Pientka, Y. Peng, F. von Oppen, B. W. Heinrich, and K. J. Franke, Tunneling processes into localized subgap states in superconductors, Phys. Rev. Lett. **115**, 087001 (2015).

[53] M. P. Anantram and S. Datta, Current fluctuations in mesoscopic systems with Andreev scattering, Phys. Rev. B **53**, 16390 (1996).

[54] P. Burset, B. Lu, S. Tamura, and Y. Tanaka, Current fluctuations in unconventional superconductor junctions with impurity scattering, Phys. Rev. B **95**, 224502 (2017).

[55] A. V. Balatsky, I. Vekhter, and J.-X. Zhu, Impurity-induced states in conventional and unconventional superconductors, Rev. Mod. Phys. **78**, 373 (2006).

[56] G. C. Ménard, S. Guissart, C. Brun, S. Pons, V. S. Stolyarov, F. Debontridder, M. V. Leclerc, E. Janod, L. Cario, D. Roditchev, P. Simon, and T. Cren, Coherent long-range magnetic bound states in a superconductor, Nat. Phys. **11**, 1013 (2015).